Tunneling giant magnetoresistance in heterogeneous Fe-SiO_2 granular films

S. Honda, T. Okada, and M. Nawate*
Physical Electronics, Faculty of Engineering, Hiroshima University, 1-4-1 Kagamiyama, Higashi-Hiroshima 739, Japan

M. Tokumoto
Electrotechnical Laboratory, 1-1-4 Umezono, Tsukuba 305, Japan
(Received 4 August 1997)

Magnetic and transport properties are examined for heterogeneous Fe-SiO_2 granular films prepared on glass substrates by rf sputtering. The superparamagnetic nature and the tunneling giant magnetoresistance are observed in the films having Fe volume fractions smaller than 45%. The magnetization and magnetoresistance (MR) curves are systematically analyzed by the summation of two Langevin functions. The dependence of the MR ratio on the Fe volume fraction is explained phenomenologically by the distance between the nearest-neighbor grain surfaces. The temperature dependence of the MR ratio is also discussed.
[S0163-1829(97)06946-4]

I. INTRODUCTION

There has been extensive interest in magnetoresistance after the discovery of the giant magnetoresistance (GMR) in Fe/Cr multilayers,[1] and subsequently in magnetic heterogeneous alloys with ferromagnetic granules embedded in a nonmagnetic metallic matrix.[2] The mechanism of GMR is believed to be based on spin-dependent scattering. A similar magnetoresistance (MR) was observed early in granular metals embedded in insulators, such as Ni-SiO_2 (Refs. 3 and 4) and Co-SiO_2,[5] and in artificial layered structures of ferromagnetic metal-insulator-metal junctions.[6] In these cases, the MR has been interpreted to be due to spin-dependent tunneling. Recently, a quite large MR has been observed in Fe/Al_2O_3/Fe (Ref. 7) and CoFe/Al_2O_3/Co or NiFe junctions,[8] and in Co-Al-O granular magnetic films,[9] and it is called tunneling GMR.

In a previous paper,[10] we discussed the magnetoresistance in Fe-SiO_2 multilayers which had the thickness ratio between Fe and SiO_2 layers ranging from 1.0 to 1.2. The largest MR ratio of 3.6% was obtained at room temperature in a film of 2 Å Fe layer thickness, and the temperature dependence of the MR ratio was weak. The weak temperature dependence was consistent with the theory given by Inoue and Maekawa.[11] On the other hand, Helman and Abeles reported that the MR ratio in Ni-SiO_2 and Co-SiO_2 heterogeneous granular films changed proportionally to the inverse of temperature, and they discussed their results theoretically.[4] In this paper, we will discuss the composition and temperature dependences of MR ratio in Fe-SiO_2 heterogeneous granular films.

II. EXPERIMENT

Heterogeneous granular Fe-SiO_2 films were prepared on glass substrates by rf sputtering at 10 mTorr Ar gas pressure from a composite target consisting of an Fe plate placed asymmetrically on a SiO_2 disk.[12] The asymmetry in target composition brought the gradient in the film composition, and then we could simultaneously obtain the samples of various compositions on a substrate with a single sputtering run.[12] The film thickness ranged from 2300 to 4000 Å. We measured the atomic compositions of Fe and Si in the films by Rutherford backscattering spectroscopy, and calculated the volume fraction of Fe, x, assuming that the densities of Fe and SiO_2 were the same as bulk values; 7.86 and 2.22 g/cm^3, respectively.

The crystalline structure was examined by the x-ray-diffraction method with Cu $K\alpha$ radiation and the film structure was observed by transmission electron microscopy (TEM). The magnetic properties were measured at room temperature (RT) with a vibrating sample magnetometer. The magnetoresistance (MR) was obtained using the dc method with in-plane field H; the maximum field H_m was 15 kOe for the data at RT and 9 kOe for the temperature dependence of MR.

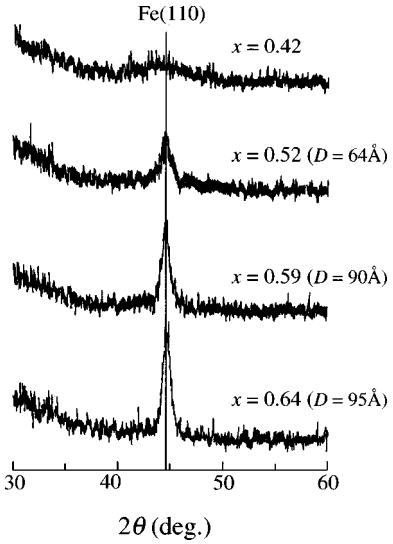

FIG. 1. X-ray-diffraction patterns for the Fe-SiO_2 films having various volume fractions, x's, measured with Cu $K\alpha$ radiation. The vertical solid line indicates the peak position corresponding to the (110) planes of bulk Fe. The value of D means the size of Fe granules evaluated from the (110) peak width.

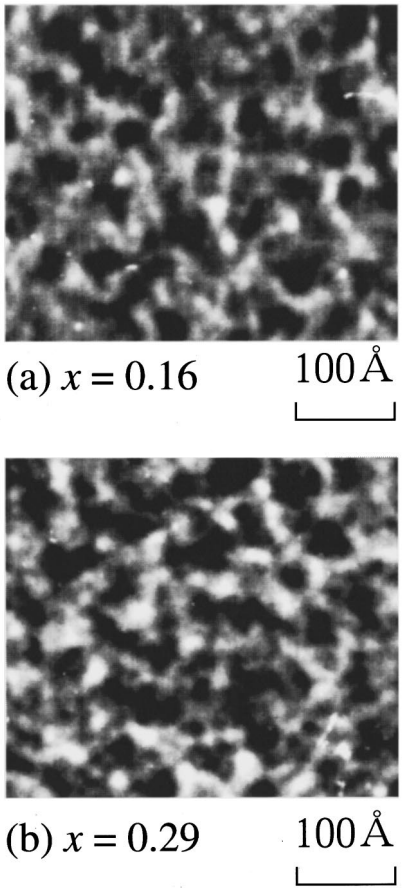

FIG. 2. TEM images of the Fe-SiO_2 films with (a) $x=0.16$ and (b) $x=0.29$.

III. RESULTS AND DISCUSSION

A. Crystalline structure and magnetic properties

Typical x-ray-diffraction patterns are shown in Fig. 1 for various Fe volume fractions x's. The bcc Fe (110) peak appears at $2\theta=44.5°$ for larger x. With decreasing x, the peak intensity weakens and the width broadens, indicating that the Fe grain size becomes smaller; from about 95 Å for $x=0.64$ to about 64 Å for $x=0.52$, which were evaluated from Scheller's formula. For $x<0.40$, the peak intensity becomes too small to be detected. Figure 2 shows the TEM images for the films of (a) $x=0.16$ and (b) 0.29. In this figure, we can clearly observe the isolated Fe granules, whose diameter is distributed between 10 and 25 Å.

Because the granules are small and isolated, the magnetization curves exhibit the superparamagnetic nature, namely show nonhysteresis and unsaturation characteristics as indicated in Fig. 3. This is consistent with the Mössbauer spectra reported by Mitani *et al.*[13] The susceptibility at zero field increases with x, because of the increase in the size of the Fe granules.

The saturation magnetizations at RT obtained from the values at 15 kOe are plotted in Fig. 4 by open circles. For $x\geqslant 0.45$, the data fit well on the solid linear line indicating that the Fe grains have the same saturation magnetization per Fe volume fraction as pure α-Fe bulk, 1714 emu/cm^3. This is consistent with the Mössbauer spectra for larger x.[13] For $x\leqslant 0.43$, the data points are slightly smaller than the solid line.

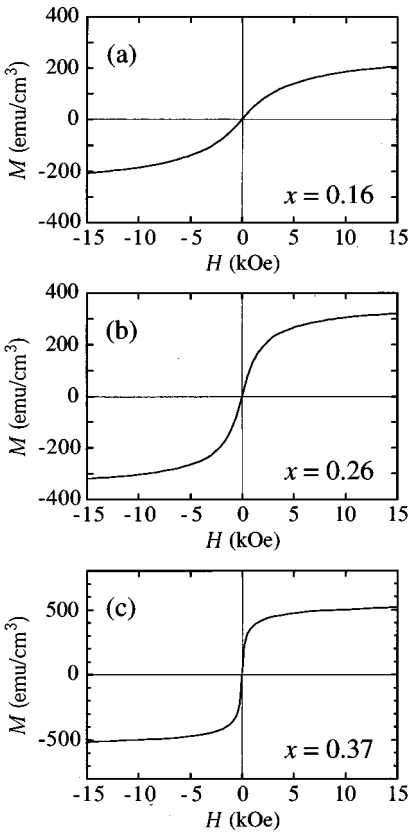

FIG. 3. In-plane magnetization curves for various volume fractions, x's, measured at room temperature.

This is probably due to the unsaturation at 15 kOe relating to the superparamagnetic nature, or the existence of the magnetically dead granules. Here, the solid circles indicate the magnetization values extrapolated to $H=\infty$ using Eq. (1) given below [see Fig. 6(a)]. The extrapolated values also are smaller than the solid line, suggesting the latter.

The magnetization curves exhibiting the superparamagnetic nature for $x\leqslant 0.43$ can be well expressed by the sum-

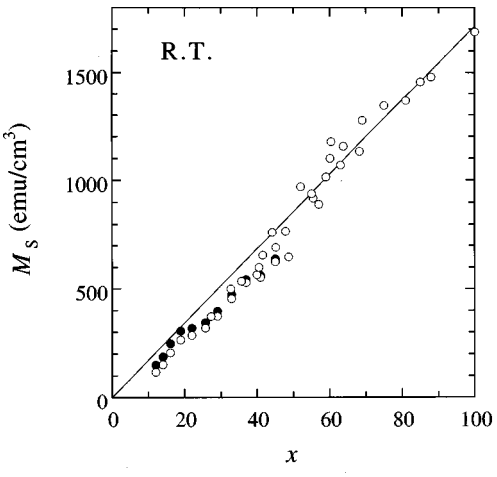

FIG. 4. Saturation magnetization M_s defined from the magnetization values at 15 kOe in-plane field as a function of x. The open circles are the experimental data measured at room temperature, and the solid circles are the values extrapolated to $H=\infty$ using Eq. (1). The solid line indicates that the magnetic moment per Fe volume M_{Fe} is constant to be 1714 emu/cm^3.

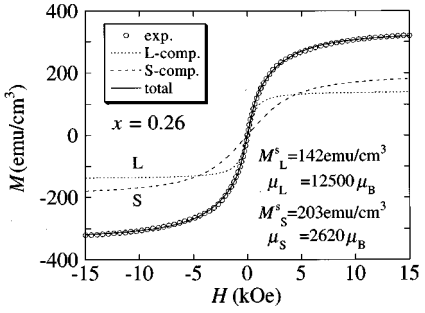

FIG. 5. Experimental and calculated magnetization curves for $x=0.26$. The circles indicate the experimental data. The solid and broken lines are the calculated values of Eq. (1) for total and S and L components, respectively.

mation of two Langevin functions, indicating that the grain size is distributed around two groups of the smaller and larger ones. Figure 5 shows an example; the analysis in the experimental magnetization curve for $x=0.26$ using two Langevin functions. Here, the open circles indicate the experimental data and the solid curve is the calculations of the following equation:

$$M(H,T)=M_S^s[\coth(\mu_S H/KT)-(kT/\mu_S H)]+M_L^s[\coth(\mu_L H/KT)-(kT/\mu_L H)]=M_S^s L_S(H,T)+M_L^s L_L(H,T), \quad (1)$$

where the subscripts S and L mean the smaller and larger grains, respectively, and M_S^s and M_L^s are the saturation magnetizations, μ_S and μ_L are the magnetic moments of unit magnetic cell of the smaller and larger granules, respectively, T is the temperature, and k is the Boltzmann constant. The broken lines indicate each term of Eq. (1) with $M_S^s=203$ emu/cm^3 and $\mu_S=2620\mu_B$ and $M_L^s=142$ emu/cm^3 and $\mu_L=12\,500\mu_B$. From the values of M_i^s and μ_i ($i=S$ and L), the number of S and L granules per unit volume are evaluated to be $N_S=8.4\times10^{18}$ cm^{-3} and $N_L=1.2\times10^{18}$ cm^{-3}, respectively.

From the x-ray diffraction and Fig. 4, we can suggest that the superparamagnetic grains are bcc crystalline structure and they have the magnetic moment of $2.22\mu_B$ per Fe atom. Then, the volume of each grain, V_i ($i=L$ or S) can be estimated by the relation, $V_i=\mu_i/2.22\mu_B a_0^{3/2}$, where $a_0=2.87$ Å is the lattice constant of bcc Fe. Assuming a spherical grain structure, the grain radii are given by $r_i=[V_i/(4\pi/3)]^{1/3}$. In Fig. 5, $r_S\cong14.9$ Å and $r_L\cong25.1$ Å are obtained, and they indicate that the size of Fe grains is distributed around 14–25 Å, consistent with the TEM observations (Fig. 2).

Thus, we can estimate the values of M_S^s and M_L^s for various x's as plotted in Fig. 6(a) by the squares and the triangles, respectively. The solid circles indicate the sums of M_S^s plus M_L^s, namely the total saturation magnetizations, which are plotted also in Fig. 4 by the solid circles. The calculated values are slightly smaller than the solid line, indicating the existence of the magnetically dead granules because of too small size. Combing the calculated values of M_i^s and μ_i, the number of grains per unit volume N_i and the radius r_i are calculated as plotted in Figs. 6(b) and 6(c). In

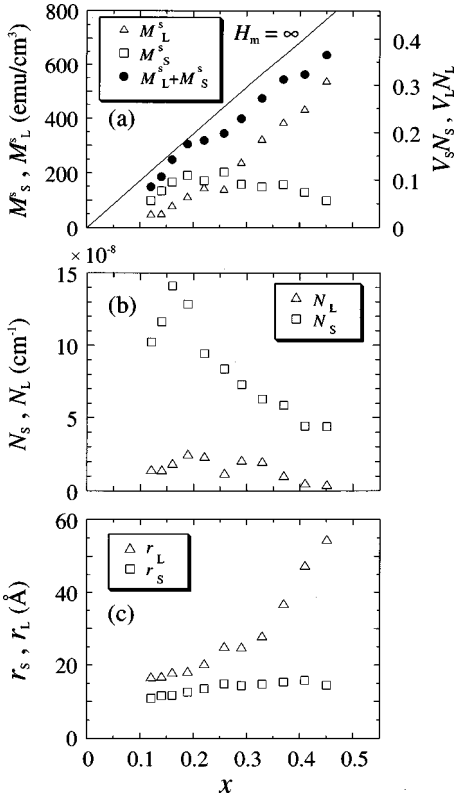

FIG. 6. Analyzed data using Eq. (1); (a) Magnetizations, M_S^s and M_L^s, or volume fractions, V_SN_S and V_LN_L, (b) densities of grains, N_S and N_L and (c) radii of grains, r_S and r_L, for S and L granules, which are plotted by the squares and the triangles, respectively. In (a), the solid circles and the solid line indicate the total magnetizations extrapolated to $H=\infty$ and the value of $M_{Fe}=1714$ emu/cm^3, respectively.

Fig. 6(a), the volume fraction N_iV_i, which is proportional to M_i^s, is scaled also at the right-hand vertical axis. As found from Fig. 6(a), the volume fraction of the L granules increases linearly with x, while that of the S granules shows the maximum at $x\approx0.17$ and then decreases gradually with increasing x. This means that the number of S granules N_S has the maximum at $x\approx0.17$ and decreases remarkably with increasing x above 0.2, while that of the L granules N_L shows the slight dependence on x, as found from Fig. 6(b). On the other hand, the value of r_S depends weakly on x: 10–15 Å, while r_L increases with x from 15 Å at $x=0.1$ to 55 Å at $x=0.45$.

B. Tunneling effect and magnetoresistance

The resistivity at zero field $\rho(0)$ increases logarithmically with decreasing x as indicated in Fig. 7, where the data agree well with the results of Ref. 13. Here, we can see the discontinuous increase at around $x=0.45$, at which the mechanism of the electrical conductivity is changed. As shown in Fig. 8, at the threshold point around $x=0.45$ the sign of the temperature coefficient of resistivity (TCR) changes. For $x\geqslant0.50$, the TCR is positive indicating the metallic conductivity, while for $x\leqslant0.45$ it becomes negative suggesting the nonmetallic conductivity such as the amorphouslike, semiconductorlike or the tunneling conductivity.

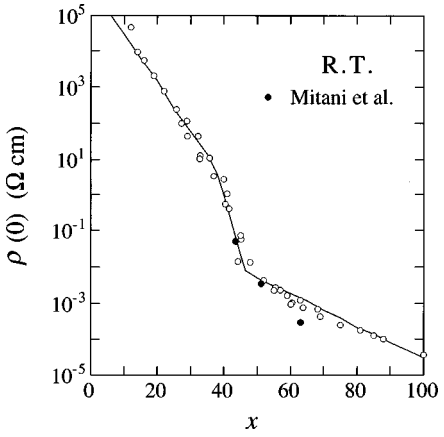

FIG. 7. Resistivity measured at room temperature with zero field $\rho(0)$ as a function of x. The solid circles are data after Ref. 13.

The tunneling conductivity in the films of granular metals embedded in the insulator has been discussed by Helman and Abeles[4] and Sheng, Abeles, and Arie;[14] the temperature dependence of $\rho(0)$ is given by

$$\rho(0)=a\ \exp\left\{2\sqrt{\frac{c}{kT}}\right\}, \tag{2}$$

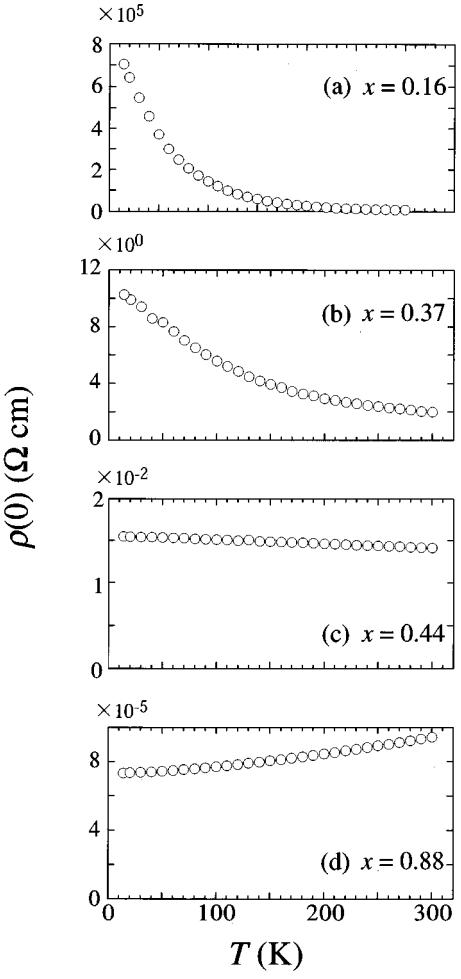

FIG. 8. Temperature dependences of $\rho(0)$ for various volume fractions x's.

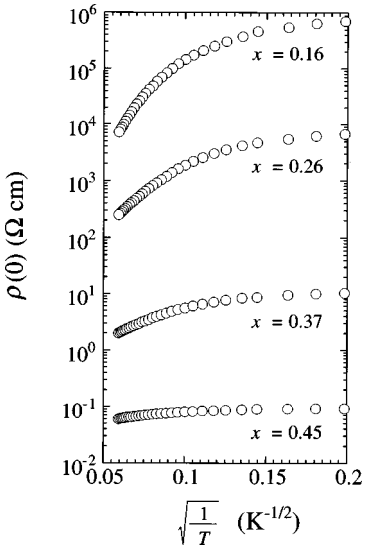

FIG. 9. Relationship between $\rho(0)$ and $1/T^{1/2}$ for various x's.

where a is the constant, and c is the activation energy proportional to both the tunnel-barrier thickness and the charging energy of the metallic grain. The experimental data of the relation between $\rho(0)$ and $1/T^{1/2}$ are plotted in semilogarithmic scale in Fig. 9. These data show the nonlinearity, indicating that the other effect is included as well as the tunneling effect.

Figure 10 shows that the data fit well on the following relation instead of Eq. (2);

$$\frac{1}{\rho(0)}=\frac{1}{\rho_t}\exp\left\{-2\sqrt{\frac{c}{kT}}\right\}+\frac{1}{\rho_c}, \tag{3}$$

where $1/\rho_t$ and $1/\rho_c$ are the constants. In Fig. 10, the circles indicate the experimental data for $x=0.26$ and the solid line indicates Eq. (3) with $1/\rho_t=0.13\ \Omega^{-1}\ \mathrm{cm}^{-1}$, $1/\rho_c=2.2\times10^{-4}\ \Omega^{-1}\ \mathrm{cm}^{-1}$ and $c=0.08$ eV. The cause of $1/\rho_c$ is not clarified at present, but it probably corresponds to the leak conductivity.

By fitting the experimental data to Eq. (3), we can obtain the constants $1/\rho_t$, $1/\rho_c$, and c as a function of x. They are plotted in Figs. 11 and 12. The values of $1/\rho_t$ show the good coincidence with those of Ni-SiO_2 granular films.[15] Furthermore, the data for c agree well with the values for Co-SiO_2,[5]

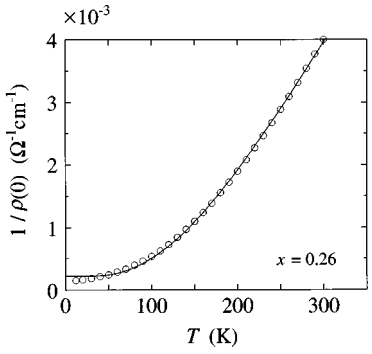

FIG. 10. Temperature dependence of $1/\rho(0)$ for $x=0.26$. The circles are the experiments and the solid line indicates Eq. (3) with $1/\rho_t=0.13\ \Omega^{-1}\ \mathrm{cm}^{-1}$, $1/\rho_c=2.2\times10^{-4}\ \Omega^{-1}\ \mathrm{cm}^{-1}$, and $c=0.08$ eV.

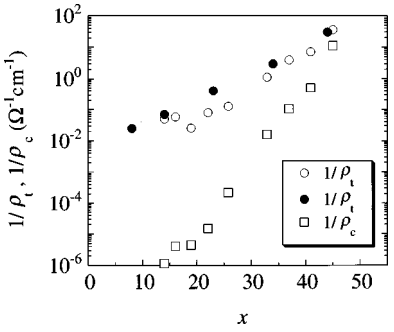

FIG. 11. Values of the constants $1/\rho_t$ (open circles) and $1/\rho_c$ (squares) versus x. The solid circles are the data for Ni-SiO_2 (Ref. 15).

Au-Al_2O_3,[15] W-Al_2O_3,[15] and Pt-SiO_2,[15] and they fit well on the solid line of the theoretical relation;

$$c=\eta\frac{[(\pi/6x)^{1/3}-1]^2}{[(\pi/6x)^{1/3}-1/2]} \tag{4}$$

with $\eta=1$ eV.[15]

The magnetoresistance (MR) curves measured at RT with in-plane fields for the same films as Fig. 4 are shown in Fig. 13, where $-\Delta\rho(H)/\rho(0)=-[\rho(H)-\rho(0)]/\rho(0)$ and $\rho(H)$ is the resistivity at field H. Similarly to the magnetization curves of Fig. 4, the MR curves exhibit the nonhysteresis and unsaturation characteristics. As x increases, the field sensitivity at lower fields increases corresponding to the increase in the susceptibility at around zero field, and the MR ratio for $H_m=15$ kOe increases up to about 3.6% at $x=0.37$.

If the tunneling occurs mainly between the nearest-neighbor grains which are equal or nearly equal in size,[4] the conductivities measured at temperature T with fields H and 0, $\sigma(H,T)$ and $\sigma(0,T)$, are given by

$$\sigma(H,T)=\sigma_S(H,T)+\sigma_L(H,T),$$
$$\sigma(0,T)=\sigma_S(0,T)+\sigma_L(0,T). \tag{5}$$

Here, the subscripts S and L mean that the tunneling occurs between S granules or L granules only. Then, the MR ratio at the field H is calculated as

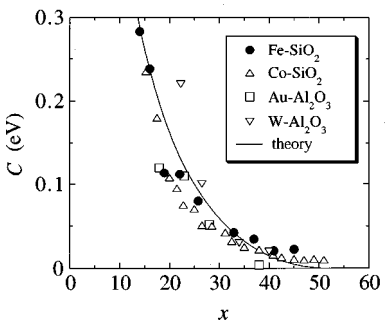

FIG. 12. Activation energy for tunneling c as a function of x. Here, the data for Co-SiO_2 (Ref. 5), Au-Al_2O_3 (Ref. 15), and W-Al_2O_3 (Ref. 15), are plotted also. The solid line indicates Eq. (4) with $\eta=1$ eV.

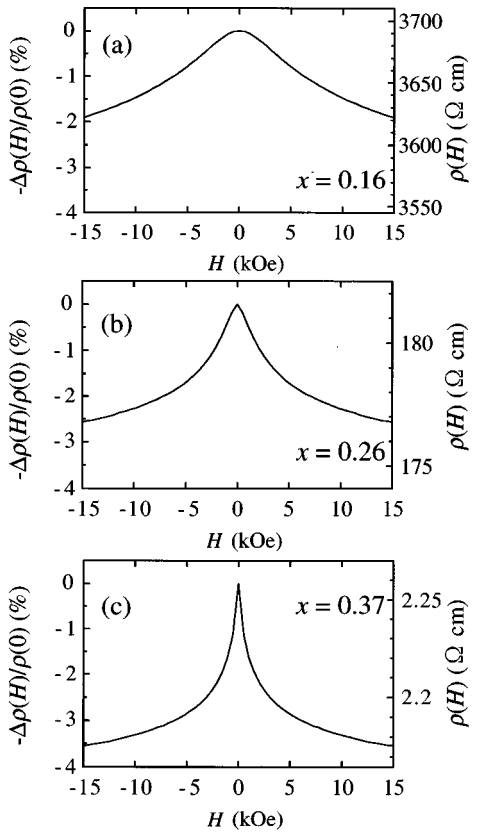

FIG. 13. MR curves measured at room temperature for various x's. The vertical axis indicates the values of $-\Delta\rho(H)/\rho(0)=-[\rho(H)-\rho(0)]/\rho(0)$ or the resistivity $\rho(H)$ at the field H.

$$\begin{aligned}\Delta\rho(H,T)/\rho(0,T)&=\frac{\rho(H,T)-\rho(0,T)}{\rho(0,T)}=\frac{\sigma(0,T)-\sigma(H,T)}{\sigma(H,T)}\\&=\frac{\sigma_S(H,T)}{\sigma(H,T)}\left[\frac{\sigma_S(0,T)-\sigma_S(H,T)}{\sigma_S(H,T)}\right]\\&\quad+\frac{\sigma_L(H,T)}{\sigma(H,T)}\left[\frac{\sigma_L(0,T)-\sigma_L(H,T)}{\sigma_L(H,T)}\right]\\&\approx G_S(T)\frac{\Delta\rho_S(H,T)}{\rho_S(0,T)}+G_L(T)\frac{\Delta\rho_L(H,T)}{\rho_L(0,T)},\end{aligned} \tag{6}$$

where $\rho(H,T)$ and $\rho(0,T)$ are the resistivities measured at temperature T with in-plane fields H and 0, and $G_S(T)$ and $G_L(T)$ are the constants. In the granular films, the tunneling probability is related to the angle between the magnetic moments of the nearest-neighbor granules and then it is proportional to the square of the magnetization; $\propto L_i^2(H,T)$, $(i=S,L)$. Therefore, from Eq. (6) the apparent magnetoresistance is given by

$$\Delta\rho(H,T)/\rho(0,T)=-A_S(T)L_S^2(H,T)-A_L(T)L_L^2(H,T), \tag{7}$$

where $L_S(H,T)$ and $L_L(H,T)$ are the Langevin functions given in Eq. (1), and $A_S(T)$ and $A_L(T)$ are the MR ratios for $H_m=\infty$ arising from the smaller and larger grains, respectively.

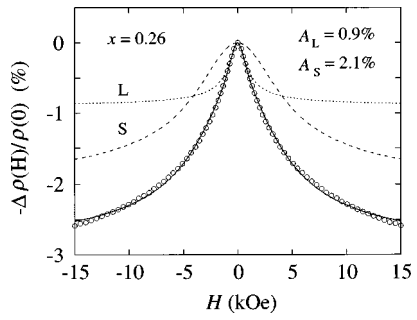

FIG. 14. Experimental and calculated MR curves for $x=0.26$. The open circles indicate the experimental data, and solid and broken lines indicate the calculations of Eq. (7) for the total and S and L components, respectively.

The MR curves can be analyzed using Eq. (7). Figure 14 shows an example for the analysis of the MR curve of Fig. 13(b), where the experimental data are plotted by the open circles. The solid line indicates Eq. (7) using the same parameters as those obtained by the analysis in Fig. 5. It is found that the good agreement is obtained between the experiments and Eq. (5). In Fig. 14, the broken lines are the calculations of each term of Eq. (7), namely the MR curves arising from the S and L granules, respectively.

The MR ratio measured at RT with $H_m=15$ kOe, $[\rho(15\ \text{kOe,RT})-\rho(0,\text{RT})]/\rho(0,\text{RT})$, is plotted by open circles in Fig. 15(a) as a function of x. The maximum value of about 3.6% is obtained at $x\approx 0.37$. For $x>0.37$, the MR ratio decreases rapidly with increasing x. Here, the solid circles indicate the results analyzed by using Eq. (7). The good agreement is obtained between the experimental data and the calculations. In Fig. 15(a), the calculated values of the MR ratio for each component in $H_m=15$ kOe are shown also. In $x\leqslant 0.37$, the values of S component show the weak dependence on x, while those of L component decrease with decreasing x. Thus, the x dependence of the total MR ratio is dominated by the L component. The calculated values for

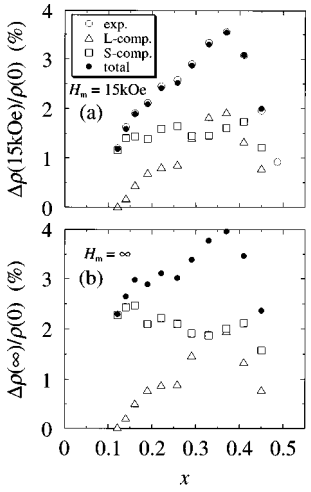

FIG. 15. Analyzed data of MR ratio using Eq. (7) for the S component (squares), L component (triangles), and the total values (solid circles) as a function of x for (a) $H_m=15$ kOe and (b) $H_m=\infty$. The open circles in (a) indicate the experimental data.

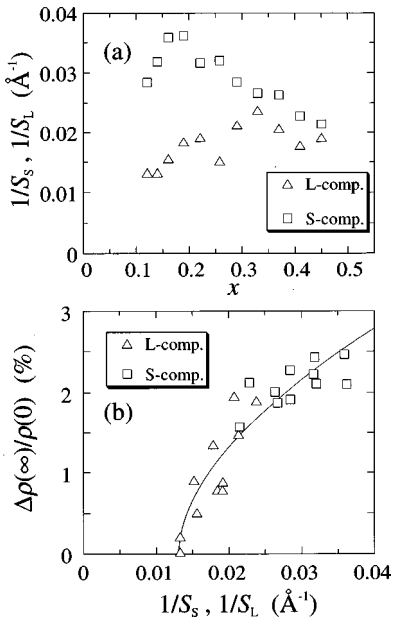

FIG. 16. (a) Inverse of the separate distances between grain surfaces, $1/S_S$ and $1/S_L$, for the S and L components as a function of x, and (b) relation between $\Delta\rho(\infty)/\rho(0)$ and $1/S_S$ or $1/S_L$.

$H_m=\infty$; A_S, A_L, and A_S+A_L are plotted in Fig. 15(b). The x dependences of A_S and A_L in $x\leqslant 0.37$ are similar to those of M_S^s and M_L^s, or N_S and N_L presented in Fig. 6, respectively. Therefore, the changes in A_S and A_L are probably related to the x dependences of the granular densities or the distances between nearest-neighboring grain surfaces.

We have calculated the separate distances, S_S and S_L, assuming that the each grain populates independently. The calculated values of $1/S_S$ and $1/S_L$ are shown in Fig. 16(a) as a function of x. It is found that the behaviors of $1/S_S$ and $1/S_L$ are similar to those of A_S and A_L. This suggests that the MR ratio is a function of the separate distance between nearest-neighbor grain surfaces as replotted in Fig. 16(b).

On the other hand, the decrease in both values of A_S and A_L in $x>0.37$ is closely related to the drastic decrease in $\rho(0)$ at around $x=0.37$ (see Fig. 7). In other words, the magnetoresistance arising from the tunneling effect becomes smaller in the range of $x>0.37$ because of the percolation effect.

C. Temperature dependence of the magnetoresistance

The temperature dependence of the MR ratio measured with $H_m=9$ kOe is shown in Fig. 17 for various x's. In the range of $x\geqslant 0.37$, the temperature dependence is very weak, while the MR ratio for $x<0.33$ increases when temperature decreases to a critical point indicated by an arrow, followed by weak temperature dependence or the decrease. The critical point shifts to lower temperature with decreasing x, suggesting that its point corresponds to the blocking temperature T_B.

An example for the temperature dependence of the magnetization curve in the film of $x=0.22$ is shown in Fig. 18 which were measured using superconducting quantum interference device. The curves at 60 K [Fig. 18(a)] are well expressed by Eq. (1) using the same parameters as those at

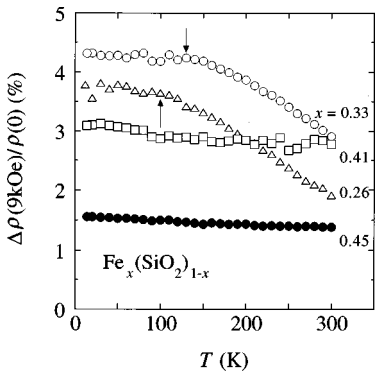

FIG. 17. Temperature dependence of the MR ratio in $H_m = 9$ kOe, $\Delta\rho(9\text{ kOe})/\rho(0)$, for various x's.

RT; $M_S^s = 149$ emu/cm^3, $\mu_S = 1089\mu_B$, $M_L^s = 170$ emu/cm^3 and $\mu_L = 4970\mu_B$, suggesting the superparamagnetic nature above 60 K, or T_B to be lower than 60 K. However, the curve at 4.2 K [Fig. 18(b)] exhibits the hysteresis, indicating the ferromagnetic nature. Here, the magnetization value at 30 kOe is higher than the value of $M_S^s + M_L^s = 320$ emu/cm^3 by a factor of about 1.5. This larger value might arise from the magnetizations of small granules which are magnetically dead at higher temperature, and from the paramagnetic component of glass substrate which is diamagnetic at higher temperature. The MR curves for the same film as Fig. 18 are presented in Fig. 19 for several temperatures. These figures indicate that in the temperatures higher than 60 K or T_B the MR curves fit well on Eq. (7) with the same parameters as those at RT, while below T_B the agreement between the experimental curves and Eq. (7) is weak because of changing in the magnetism. In these figures, the coefficients A_S and A_L are given for each temperature.

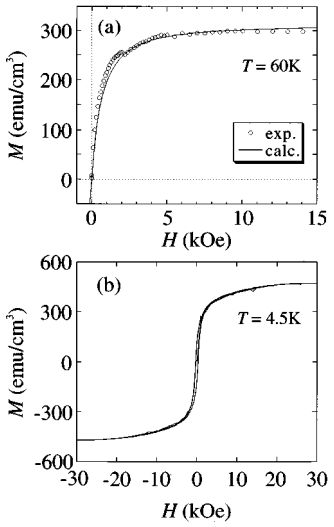

FIG. 18. In-plane magnetization curves of the film with $x = 0.22$ measured at (a) 60 K and (b) 4.5 K. In (a), the open circles are the experimental data and the solid line indicates the calculations of Eq. (1) with $M_S^s = 149$ emu/cm^3, $\mu_S = 1089\mu_B$. $M_L^s = 170$ emu/cm^3 and $\mu_L = 4970\mu_B$, which were obtained from the magnetization curve measured at room temperature. In (b), only the experimental curve is shown.

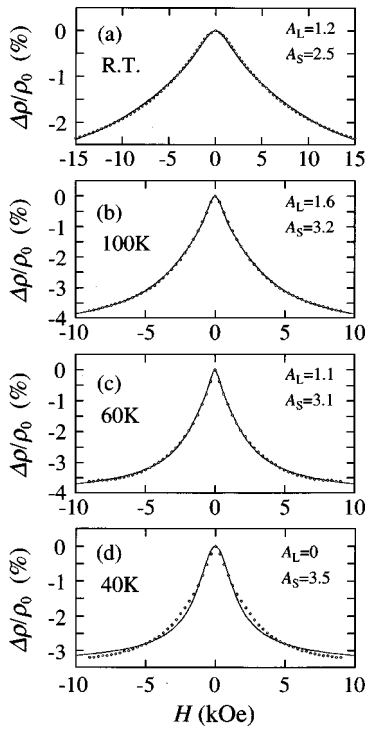

FIG. 19. MR curves at various temperatures for the same film as Fig. 18 ($x = 0.22$). The open circles and the solid lines indicate the experimental data and the calculations of Eq. (7), respectively. In the calculations, the same parameters as those in Fig. 18(a) were used.

Thus, the values of $A_S(T)$ and $A_L(T)$ can be evaluated for various temperatures. The data and their sum are plotted in Fig. 20(a) for the same film as Fig. 19. Here, the experimental data for $H_m = 9$ kOe are plotted also by the open circles. As found from Fig. 20(a), the temperature dependence of

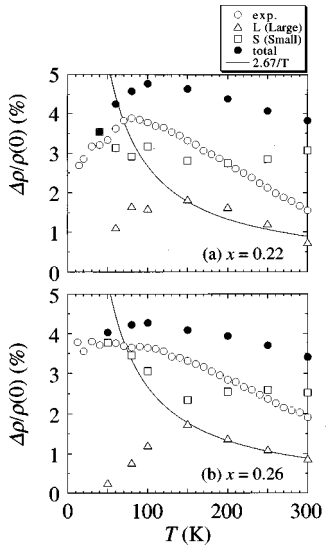

FIG. 20. Temperature dependences of the MR ratio for (a) $x = 0.22$ and (b) $x = 0.26$. The solid circles, squares, and triangles are the calculations for the total, S and L components of the MR ratio in $H_m = \infty$, respectively, and the open circles are the experimental data in $H_m = 9$ kOe. The solid lines indicate the relation of $\Delta\rho(\infty)/\rho(0) \propto 1/T$.

$A_S(T)$ is very weak, consistent with the theory proposed by Inoue and Maekawa.[11] However, the $A_L(T)$ depends strongly on temperature; with decreasing temperature, the $A_L(T)$ increases slightly until 150 K and then decreases rapidly to zero. The decrease in $A_L(T)$ is probably caused by the increase in the exchange interaction between the nearest-neighbor granules. This interaction suppresses the random orientation of the magnetic moment at zero field, resulting in the low resistivity at zero field and also lowering the MR ratio. For higher temperature, the $A_L(T)$ approximately follows the relation proportional to $1/T$, which was given by Helman and Abeles,[4] and which is indicated by the solid line.

Another example is shown in Fig. 20(b) for $x=0.26$. In this case, the $A_S(T)$ increases with $1/T$ below 150 K, while its value above 150 K is almost constant. Thus, the lower temperature values of $A_S(T)$ and the higher temperature values of $A_L(T)$ agree well with the relation of $1/T$. However, the lower temperature values of $A_L(T)$ decreases to zero with temperature similarly to Fig. 20(a).

IV. CONCLUSION

We examined the magnetic and transport properties of heterogeneous Fe-SiO_2 granular films. The superparamagnetic nature and the tunneling GMR appeared for $x \leqslant 0.45$. The magnetization and MR curves were systematically analyzed by two Langevin functions, assuming the granular size was distributed around two mean values, the smaller and larger radii r_S and r_L. The x dependence of the MR ratio was explained phenomenologically by the distance between the nearest-neighbor granular surfaces. The temperature dependence of the MR ratio was very complex; the MR ratio changed with $1/T$ at lower temperatures for the smaller granules and at higher temperatures for the larger granules.

ACKNOWLEDGMENTS

The authors are grateful to F. Nishiyama for the RBS measurements. This research was partly supported by a Grant-in-Aid for Science Research for the Ministry of Education, Culture and Science of Japan.

*Present address: CRC, Shimane University, 1060 Nishikawatsu, Matsue 690, Japan.

[1] M. N. Baibich, J. M. Broto, A. Fert, F. Nguyen Van Dau, F. Petroff, P. Etienne, G. Creuzet, A. Friederich, and J. Chazelas, Phys. Rev. Lett. **61**, 2472 (1988).

[2] J. Q. Xiao, J. S. Jiang, and C. L. Chien, Phys. Rev. Lett. **68**, 3749 (1992); C. L. Chien, J. Q. Xiao, and J. S. Jiang, J. Appl. Phys. **73**, 5309 (1993).

[3] J. I. Gittleman, Y. Goldstein, and S. Bozowski, Phys. Rev. B **5**, 3609 (1972).

[4] J. S. Helman and B. Abeles, Phys. Rev. Lett. **37**, 1429 (1976).

[5] S. Barzilai, Y. Goldstein, I. Balberg, and J. S. Helman, Phys. Rev. B **23**, 1809 (1981).

[6] S. Maekawa and U. Gäfvert, IEEE Trans. Magn. **MAG-18**, 707 (1982).

[7] T. Miyazaki and N. Tezuka, J. Magn. Magn. Mater. **151**, 403 (1995).

[8] J. S. Moodera, L. R. Kinder, T. M. Wong, and R. Meservey, Phys. Rev. Lett. **74**, 3273 (1995).

[9] H. Fujimori, S. Mitani, and S. Ohnuma, Mater. Sci. Eng. B **31**, 219 (1995).

[10] S. Honda, T. Okada, and M. Nawate, J. Magn. Magn. Mater. **165**, 153 (1996).

[11] J. Inoue and S. Maekawa, Phys. Rev. B **53**, 11 927 (1996).

[12] S. Honda, M. Nawate, M. Tanaka, and T. Okada, J. Appl. Phys. **82**, 764 (1997).

[13] S. Mitani, H. Fujimori, S. Furukawa, and S. Ohnuma, J. Magn. Magn. Mater. **140-144**, 429 (1995).

[14] Ping Sheng, B. Abeles, and Y. Arie, Phys. Rev. Lett. **31**, 44 (1973).

[15] B. Abeles, P. Sheng, M. D. Coutts, and Y. Arie, Adv. Phys. **24**, 407 (1975).